

A Viscous and Heat Conducting Ghost Fluid Method for Multi-Fluid Simulations

Steven Jöns^a, Christoph Müller^a, Johanna Hintz^a, Andrea Beck^a,
Claus-Dieter Munz^a

^a*Institute of Aerodynamics and Gas Dynamics, University of Stuttgart, 70569 Stuttgart,
Germany*

Abstract

The ghost fluid method allows a propagating interface to remain sharp during a numerical simulation. The solution of the Riemann problem at the interface provides proper information to determine interfacial fluxes as well as the velocity of the phase boundary. When considering two-material problems, the initial states of the Riemann problem belong to different fluids, which may have different equations of states. In the inviscid case, the solution of the multi-fluid Riemann problem is an extension of the classical Riemann problem for a single fluid. The jump of the initial states between different fluids generates waves in both fluids and induces a movement of the interface, similar to a contact discontinuity. More subtle is the extension to viscous and heat conduction terms which is the main focus of this paper. We account for the discontinuous coefficients of viscosity and heat conduction at the multi-fluid interface and derive solutions of the Riemann problem for these parabolic terms, from which we can derive parabolic, interfacial fluxes.

Email address: steven.joens@iag.uni-stuttgart.de (Steven Jöns)

We demonstrate the accuracy, robustness and applicability of this approach through a variety of test cases.

Keywords:

1. Introduction

In the numerical computation of multi-material and multiphase flows, a great challenge is to model the behavior of the interfaces correctly. This includes for many technical applications beside the movement of the interfaces also surface tension, viscous effects and heat conduction. All these interfacial phenomena may strongly influence the fluid flow in large parts of the surrounding region. Hence, key aspect of any numerical two-phase method is the correct balancing of all interfacial forces and fluxes such that it accurately predicts the physics. We restrict ourselves in the following to two fluids or two phases of a fluid without taking into account phase transitions. For simplicity, we name the two different fluids liquid and gas, which is our main field of application.

In general, one can distinguish between two different classes of numerical methods for two-material or two-phase flows within a continuum description: diffuse-interface (DI) and sharp-interface (SI) methods. In the DI methods, the interface in the macroscopic formulation is assumed to have a finite thickness. Specifying a continuous variation of the states in a mixing zone, the interfacial region is smeared out over a couple of grid cells, which then allows an application of a standard continuum approximation method. In this case, the inclusion of viscous and thermal terms, which depend on the gradients, is in principle straightforward. However, since the thermodynamic properties

at the different sides of the interface may strongly differ and the separate states may obey different equations of state, it is often difficult to establish the thermodynamic consistency of the mixture state and the proper behavior in the vicinity of the interface. Additionally, heat conduction and viscous effects may be difficult to approximate in a physical consistent way because of the artificially diffused interface. In physics the width of the transition zone may be in the order of a few molecules and far away from its approximate counterpart.

The SI class of methods assumes that the material interface between the fluids is infinitely thin on the macroscopic scale, which results in a discontinuity within a macroscopic continuum description. A method to keep a propagating interface sharp is to move the grid according to the interface motion. Other sharp-interface methods rely on an interface reconstruction, cut-cells or the ghost fluid method ([1]). In the latter cases, the solution of the flow equations have to be combined with a tracking of the interface movement. Several successful methods have been developed in the past including the volume-of-fluid ([2]), the front-tracking ([3]), and the level-set methods ([4]). Beside the interface tracking, the imposing of coupling conditions at the interface is another building block in the sharp-interface approach. This coupling consists of a set of jump conditions for the macroscopic variables, modelling the local physical behavior. Jump conditions may be obtained from the solution of the Riemann problem for multi-material or multiphase flow.

Due to the discontinuous nature of the physical quantities at the interface in the SI approach, the inclusion of viscous and thermal effects are challenging. This topic was addressed by Fedkiw et al. in [5] by extending the ghost

fluid methodology to the viscous stress tensor. The artificial ghost states are derived from a splitting of the viscous tensor in continuous and discontinuous terms. The gradients across the interface are evaluated by assuming a continuous transition, while the tangential terms are approximated in an upwind fashion. Another approach is the continuous surface force method, which approximates the parabolic terms by imposing continuity and regularizing the δ -function in a small neighborhood ([6, 4]). Hence, the viscous terms are reformulated from a surface force to a volume force as was done for the surface tension force in [4]. This new source term is only non-zero in a narrow band around the interface and smears the originally singular force out in this area. Both methods rely on a decomposition of the viscous stress tensor in a continuous and discontinuous part with a standard finite difference approximation for the continuous gradient calculation and with some complex workaround for the discontinuous part.

The approach under consideration in this paper is motivated by the use of the Riemann problem in the ghost fluid method for the hyperbolic terms as proposed in [7, 8, 9]. We extend the diffusive Riemann solver of Gassner et al. [10, 11] to the two-fluid case and propose a thermal and a viscous Riemann solver. According to Godunov's idea for hyperbolic conservation equations, the local solution is used to determine a numerical flux. Gassner et al. derived in [10] an exact Riemann solver for the scalar, linear diffusive generalized Riemann problem and introduced a linearization for the nonlinear case. In [11], this methodology was successfully applied to the compressible Navier-Stokes equations. In [12] it was additionally analyzed in combination with discontinuous Galerkin schemes. When using this approach, no prelim-

inary deconstruction of the viscous stress tensor nor a continuity assumption approximating the gradient across the interface is needed. The Riemann solvers are validated as building blocks in a sharp-interface level-set ghost fluid method to calculate interfacial diffusive fluxes.

As already mentioned, we restrict ourselves to the two-fluid case without phase transition. For simplicity, we name the different phases liquid and gas. The paper has a simple structure as follows: In Section 2, we discuss the governing equations and all the basic building blocks of our numerical approach. Afterwards, we describe our modification of the ghost fluid method in section 3. Here, we define Riemann solvers for heat conduction and friction. In section 4 we validate our method and apply it to test cases. Finally, we conclude our results in section 5.

2. Fundamentals

In the present section, the governing equations and the fundamental building blocks of the employed numerical scheme are introduced.

2.1. Governing Equations

We consider compressible, viscous and heat conducting two fluid flows without phase transition. The fluid flow in each phase can be described by the Navier-Stokes equations (NSE):

$$\frac{\partial \mathbf{U}}{\partial t} + \sum_{i=1}^3 \frac{\partial}{\partial x_i} [\mathbf{F}_h^i - \mathbf{F}_p^i] = 0 \quad (1)$$

with the state vector

$$\mathbf{U} = \mathbf{U}(\mathbf{x}, t) = \begin{pmatrix} \rho \\ m_1 \\ m_2 \\ m_3 \\ E \end{pmatrix} = \begin{pmatrix} \rho \\ \rho v_1 \\ \rho v_2 \\ \rho v_3 \\ \rho e \end{pmatrix}, \quad (2)$$

the hyperbolic flux

$$\mathbf{F}_h^i = \mathbf{F}_h^i(\mathbf{U}) = \begin{pmatrix} \rho v_i \\ \rho v_1 v_i + \delta_{1i} p \\ \rho v_2 v_i + \delta_{2i} p \\ \rho v_3 v_i + \delta_{3i} p \\ (\rho e + p) v_i \end{pmatrix} \quad (3)$$

and the parabolic flux

$$\mathbf{F}_p^i = \mathbf{F}_p^i(\mathbf{U}, \nabla \mathbf{U}) = \begin{pmatrix} 0 \\ \tau_{1i} \\ \tau_{2i} \\ \tau_{3i} \\ \sum_{j=1}^3 \tau_{ij} v_j - q_i \end{pmatrix}. \quad (4)$$

Thereby, the density ρ , the momentum $\mathbf{m} = (m_1, m_2, m_3)^T$ and the total energy per unit volume E are the conserved variables. Additional quantities are the velocity $\mathbf{v} = \mathbf{m}/\rho$, the total energy per unit mass $e = E/\rho$ and the pressure p . Furthermore, the viscous stress tensor is defined as

$$\underline{\boldsymbol{\tau}} = \mu \left(\nabla \mathbf{v} + (\nabla \mathbf{v})^T - \frac{2}{3} (\nabla \cdot \mathbf{v}) \underline{\underline{I}} \right) \quad (5)$$

and the heat flux is given by

$$\mathbf{q} = \begin{pmatrix} q_1 \\ q_2 \\ q_3 \end{pmatrix} = -\lambda \nabla T \quad (6)$$

with the dynamic viscosity $\mu = \mu(\rho, T)$, the thermal conductivity $\lambda = \lambda(\rho, T)$ and the temperature T . The total energy is the sum of internal and kinetic energy

$$E = \rho e = \rho \epsilon + \frac{1}{2} \rho \mathbf{v} \mathbf{v}^T \quad (7)$$

with the internal energy per unit mass ϵ . The equation system (1) is closed by an equation of state (EOS):

$$\epsilon = \epsilon(\rho, T), \quad (8)$$

$$p = p(\rho, T) \quad (9)$$

that relates the internal energy per unit mass and the pressure to density and temperature.

2.2. Sharp-Interface Method

In the following, we give a short overview of the employed sharp-interface method. It is based upon three basic building blocks: The bulk phase flow solver, the interface capturing and the ghost fluid method. A more detailed discussion can be found in [13]. We discretize the computational domain into C_n hexahedral grid cells. The fluid flow in the bulk, described by the NSE, is solved with the discontinuous Galerkin spectral element method (DGSEM), detailed in Hindenlang et al. [14] and Kraus et al. [15]. The DGSEM is a

high-order method with a tensor-product based polynomial solution representation of degree N in each grid element. The individual elements are coupled via Riemann solvers, similar to the well-known finite volume (FV) methods. The DGSEM is supplemented by the second order FV shock capturing scheme [16] which reinterprets a grid element into a set of $(N + 1)^d$ equidistantly spaced FV sub-cells. In this way strong gradients, e.g., shock waves, in the solution can be captured, avoiding spurious oscillations of the DG polynomial. Solution gradients for the parabolic terms are obtained via the BR1-lifting procedure of Bassi and Rebay [17]. Time integration is performed using an explicit fourth order low storage RK scheme [18].

The position of the interface is tracked via the level-set method of Sussman et al. [4]. Therein, the interface is defined as the zero of the level-set function $\phi(\mathbf{x}, t)$, which is a signed distance function. Advection of the interface is treated via an additional advection equation, the level-set transport equation

$$\frac{\partial \phi(\mathbf{x}, t)}{\partial t} + \sum_{i=1}^3 v_i^{\text{LS}}(\mathbf{x}, t) \frac{\partial \phi(\mathbf{x}, t)}{\partial x_i} = 0, \quad (10)$$

with v_i^{LS} being the level-set transport velocity in direction i . The numerical treatment of Eq. (10) follows Jöns et al. [13], in using the path-conservative approach of Dumbser and Loubère [19] within the DGSEM with FV shock-capturing. In this way, also the level-set field is obtained with high-order accuracy. From $\phi(\mathbf{x}, t)$, geometrical properties of the interface as normal vectors can be calculated, as discussed in [13, 20]. The advection of the level-set field does not conserve the signed-distance property, therefore it is enforced

additionally via a reinitialization procedure. Here we follow the approach of Peng et al. [21] in using a 5th-order WENO scheme to solve a Hamilton-Jacobi type equation. A similar procedure is used to obtain the level-set advection velocity [21], which is initially only known at the interface and needs to be extrapolated into the volume.

Finally, the ghost fluid Method (GFM) [1] is used to couple the individual phases with each other. In order to apply the GFM, we employ a domain decomposition based on the sign of the level-set function which identifies a grid element as liquid or vapor. In grid elements, where an interface is present, the switch to FV sub-cells is applied and the phase of each sub-cell is identified as shown in Fig. 1. This procedure thus defines a numerical interface, denoted as the surrogate phase interface, which is the discrete representation of the level-set function and coincides with the sub-cell sides. In the ghost fluid method, ghost states or ghost fluxes are introduced across these interfacial sides as boundary conditions for the bulk solver in the gas as well as in the liquid. In this way, time evolution of each phase becomes trivial if the states of the ghost fluid are known. These need to be defined in such a manner that they model the interaction at the multi-fluid interface appropriately. For the definition of the ghost state, we do not follow the original variant of Fedkiw et al. [1] but employ the Riemann solver technique as introduced in Liu et al. [7], Merkle and Rohde [8], Fechter et al. [9]. For the multi-fluid case, the GFM based on solution of Riemann problems at the interface have been considered in Xu and Liu [22], Xu et al. [23], Fechter and Munz [24]. The solution of the Riemann problem is used to define the ghost states as well as the level-set transport velocity at the interface.

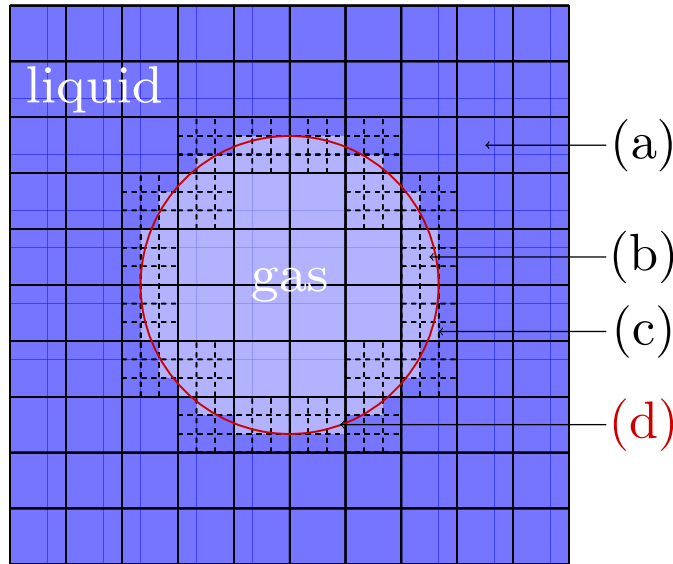


Figure 1: 2D domain decomposition: DG elements (a), FV sub-cells (b), the surrogate phase boundary (c) and the actual phase boundary (d), which is identified by the root of the level-set function, are shown.

3. A Hyperbolic-Parabolic Extension of the Ghost Fluid Method

The ghost fluid method, in which the ghost states are calculated by solving Riemann problems, has originally been considered for purely hyperbolic equation systems. In the present section, we extend it to the Navier-Stokes equations. We note that this procedure is more general and may be also applied to other hyperbolic-parabolic equation systems. Instead of ghost states, from which the numerical fluxes are calculated, we formulate the method by directly defining interfacial ghost fluxes as used in Fechter et al. [9]. Note that, when employing an exact Riemann solver in the hyperbolic case, both approaches are identical. The interfacial fluxes are written as the sum of the

hyperbolic, the viscous and the thermal flux:

$$\mathbf{F}^* = \mathbf{F}_{Euler}^* + \mathbf{F}_{Therm}^* + \mathbf{F}_{Visc}^*. \quad (11)$$

As usual in the single fluid case, the three contributions are calculated separately from each other. All interfacial fluxes are calculated by employing appropriate Riemann solvers. Before solving the parabolic Riemann problems we need an additional step. The parabolic fluxes depend on gradients at the interface. Hence, beside the states we need the gradients from the liquid and from the vapor region. On each side of the interface, the gradient is calculated based on solely the information from the same phase, allowing a jump in the gradients. We calculate these gradients by a masked least squares method, based on the approach of [25]. All entries in the least squares matrix pertaining to the opposite phase are set to zero and a one-sided gradient is calculated. These gradients are then further used as initial conditions for the Riemann problem or generalized Riemann problem as often called in the hyperbolic case for piecewise linear initial data. As usual, we use the rotational invariance of the Navier-Stokes equations, which allows us to consider one-dimensional Riemann problems into the normal direction ξ with respect to the surrogate phase boundary. We rotate the states in such a way that the left state is always liquid and the right state is always gas.

The main novelty and hence, the focus of this work, lies in the use of Riemann problems for heat conduction and friction at the interface. The use of Riemann problems for parabolic terms, similar to its hyperbolic counterpart in classical FV methods, was introduced by Gassner et al. [10] in the form of the diffusive generalized Riemann problem (dGRP) in the scalar case. The authors solved a piecewise polynomial Riemann problem exactly

and used this time dependent exact solution to define a numerical diffusion flux. Follow up investigations of Lörcher et al. [12] and Gassner et al. [11] considered heat conduction with varying diffusion coefficients as well as the application to the NSE. Given the differences in density across the interface, the mentioned approaches can not be straightforwardly applied to the sharp-interface situation considered in this paper. Hence, we extend the work from [11, 10, 12] in the following. We begin by considering a general scalar diffusion equation with jumping diffusion coefficients and derive a solution for this Riemann problem. This general solution is then used to obtain solutions of the thermal and viscous Riemann problem and fluxes for the ghost fluid method. We shortly describe the hyperbolic flux for completeness.

3.1. The Interfacial Riemann Solver for the Hyperbolic Terms

The hyperbolic Riemann problem is defined by the Euler equations

$$\mathbf{U}_t + \mathbf{F}_{Euler}(\mathbf{U})_\xi = 0 \quad (12)$$

with the piecewise constant initial data

$$\mathbf{U}(\xi, t) = \begin{cases} \mathbf{U}_{liq} & \text{for } \xi < 0, \\ \mathbf{U}_{vap} & \text{for } \xi \geq 0, \end{cases} \quad (13)$$

where ξ denotes the direction normal to the interface. The solution to this problem is obtained via the variant of the HLLC Riemann solver of Toro [26] for fluid interfaces, which was proposed by Hu et al. [27]. The assumed wave pattern for this solution is depicted in Fig. 2. It consists of two outer waves and a material interface that separates the two inner states. Surface tension may be included similar to Jaegle et al. [28] at the intermediate wave in form of the Young-Laplace Law.

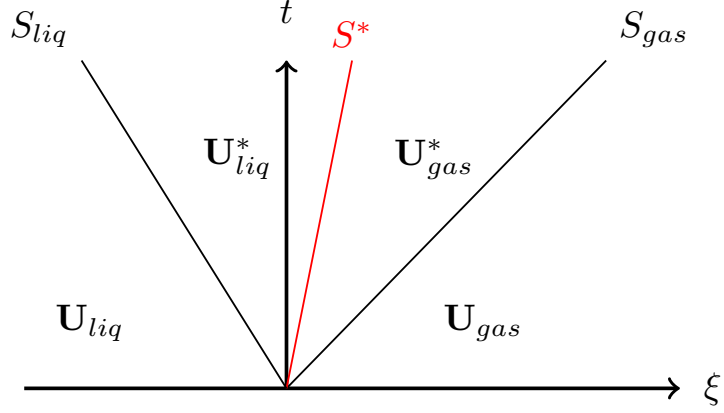


Figure 2: Approximate hyperbolic two-phase Riemann solution (HLLC).

3.2. The Generalized Scalar Riemann Problem for Diffusion with Discontinuous Coefficients

We first consider a scalar, one-dimensional diffusion equation

$$u_t - (au_\xi)_\xi = 0 \quad (14)$$

with the diffusion coefficient a . We want to solve the generalized Riemann problem with piecewise linear initial data

$$u(\xi, t = 0) = \begin{cases} u^- + \xi u_\xi^- & \text{for } \xi < 0, \\ u^+ + \xi u_\xi^+ & \text{for } \xi \geq 0, \end{cases} \quad (15)$$

with the positive and piecewise constant diffusion coefficient

$$a(\xi) = \begin{cases} a^- & \text{for } \xi < 0, \\ a^+ & \text{for } \xi \geq 0. \end{cases} \quad (16)$$

To solve this initial value problem, we follow Lörcher et al. [12] and apply the Laplace transformation to equation (14). Denoting Θ as the Laplace transform of u

$$\mathcal{L}\{u(\xi, t)\} = \Theta(\xi, s), \quad (17)$$

the transformation of (14) reads as

$$\partial_\xi^2 \Theta - \frac{s}{a} \Theta = -\frac{u^- + \xi u_\xi^-}{a}. \quad (18)$$

The solutions to this ordinary differential equation is given by

$$\Theta = c \exp\left(\sqrt{\frac{s}{a}} \xi\right) + \frac{u^-}{s} + \frac{u_\xi^-}{s} \xi \quad \text{for } \xi < 0, \quad (19)$$

with $c = c(\xi)$ being constant at each side of the interface. The values are obtained by applying compatibility conditions at the interface, $\xi = 0$:

$$\Theta^-(0, s) = \Theta^+(0, s), \quad (20)$$

$$b^- \frac{\partial}{\partial \xi} \Theta^-(0, s) = b^+ \frac{\partial}{\partial \xi} \Theta^+(0, s). \quad (21)$$

The first condition imposes the continuity of the solution. The second condition imposes the continuity of a flux. This condition is a more general than the one used by Lörcher et al. [12], where solely the continuous diffusion flux with $b^- = a^-$ and $b^+ = a^+$ was imposed. This allows us to extend this solution to the multi-fluid situation, as will be seen later. From the two conditions Eqs. (20) and (21), the coefficients c^- and c^+ for $x < 0$ and $x \geq 0$, respectively, can be determined as

$$c^- = \frac{b^+ \sqrt{a^-} (u^+ - u^-) + \sqrt{\frac{a^+ a^-}{s}} (b^+ u_\xi^+ - b^- u_\xi^-)}{s(b^+ \sqrt{a^-} + b^- \sqrt{a^+})}, \quad (22a)$$

$$c^+ = \frac{-b^- \sqrt{a^+} (u^+ - u^-) + \sqrt{\frac{a^+ a^-}{s}} (b^+ u_\xi^+ - b^- u_\xi^-)}{s(b^+ \sqrt{a^-} + b^- \sqrt{a^+})}, \quad (22b)$$

giving the solution of the dGRP. To calculate the numerical flux from this solution, we need the derivatives of Θ from Eq. (19) with respect to ξ :

$$\left(\frac{\partial}{\partial \xi}\Theta^-\right)(\xi, s) = c^- \sqrt{\frac{s}{a^-}} \exp\left(\sqrt{\frac{s}{a^-}}\xi\right) + \frac{u_\xi^-}{s}, \quad (23a)$$

$$\left(\frac{\partial}{\partial \xi}\Theta^+\right)(\xi, s) = -c^+ \sqrt{\frac{s}{a^+}} \exp\left(-\sqrt{\frac{s}{a^+}}\xi\right) + \frac{u_\xi^+}{s}. \quad (23b)$$

Applying the inverse Laplacian, we obtain the physical derivatives as

$$\frac{\partial}{\partial \xi}u^-(0, t) = \frac{b^+(u^+ - u^-)}{\sqrt{\pi t}(b^+\sqrt{a^-} + b^-\sqrt{a^+})} + \frac{\sqrt{a^+}b^+u_\xi^+ + b^+\sqrt{a^-}u_\xi^-}{b^+\sqrt{a^-} + b^-\sqrt{a^+}}, \quad (24)$$

$$\frac{\partial}{\partial \xi}u^+(0, t) = \frac{b^-(u^+ - u^-)}{\sqrt{\pi t}(b^+\sqrt{a^-} + b^-\sqrt{a^+})} + \frac{\sqrt{a^+}b^-u_\xi^+ + b^-\sqrt{a^-}u_\xi^-}{b^+\sqrt{a^-} + b^-\sqrt{a^+}}. \quad (25)$$

From these solution gradients, we obtain the numerical diffusion flux by taking the integral mean in time for one time step

$$\mathbf{G} = \frac{1}{\Delta t} \int_0^{\Delta t} b \frac{\partial u}{\partial \xi}(0, t) dt. \quad (26)$$

We note that the derivatives are singular at $\xi = 0$ as derivatives of a discontinuous function. However, the time average exists as an improper integral and reads as

$$\mathbf{G} = \frac{2b^+b^-(u^+ - u^-)}{\sqrt{\pi\Delta t}(b^+\sqrt{a^-} + b^-\sqrt{a^+})} + \frac{b^+b^-(\sqrt{a^+}u_\xi^+ + \sqrt{a^-}u_\xi^-)}{(b^+\sqrt{a^-} + b^-\sqrt{a^+})}. \quad (27)$$

From Eq. (27), the case studied by Lörcher et al. [12] is recovered for $b^- = a^-$ and $b^+ = a^+$.

3.3. The Numerical Heat Flux

In the following, we want to derive a formulation for the numerical heat flux. Therefore, we want to solve the thermal Riemann problem normal to

the interface defined by

$$\mathbf{U}_t - \mathbf{F}_{Therm}(\mathbf{U})_\xi = 0, \quad (28)$$

with the thermal flux $\mathbf{F}_{Therm}(\mathbf{U}) = (0, 0, 0, -q_1)^T$, and the piecewise linear initial data

$$\mathbf{U}(\xi, t = 0) = \begin{cases} \mathbf{U}_{liq}^- + \xi (\mathbf{U}_{liq})_\xi^- & \text{for } \xi < 0 \\ \mathbf{U}_{gas}^+ + \xi (\mathbf{U}_{gas})_\xi^+ & \text{for } \xi \geq 0 \end{cases}. \quad (29)$$

We further assume both time independence and a piecewise constant distribution of the thermal conductivity λ and the specific heat at constant volume c_v . Eq.(28) is identical to considering the energy equation

$$\frac{\partial}{\partial t} (\rho\epsilon)_t + \frac{\partial}{\partial \xi} \left(\lambda \frac{\partial}{\partial \xi} T \right) = 0 \quad (30)$$

under the condition of a time independent density and momentum. In the following, we reformulate Eq. (30) to an equation for the temperature in order to receive a connection with the numerical flux constructed in the previous subsection. We utilize the thermodynamic identity

$$d\epsilon = \left(\frac{\partial \epsilon}{\partial T} \right)_\rho dT + \left(\frac{\partial \epsilon}{\partial \rho} \right)_T d\rho \quad (31)$$

$$= c_v dT + \left(\frac{\partial \epsilon}{\partial \rho} \right)_T d\rho, \quad (32)$$

and obtain

$$\frac{\partial}{\partial t} (\rho c_v T) + \frac{\partial}{\partial \xi} \left(\lambda \frac{\partial}{\partial \xi} T \right) = 0. \quad (33)$$

With the assumptions on λ and c_v we can formulate the temperature equation as

$$\frac{\partial T}{\partial t} + k \frac{\partial^2}{\partial \xi^2} T = 0, \quad (34)$$

with the thermal diffusivity

$$k = \frac{\lambda}{\rho c_\nu}. \quad (35)$$

Reinterpreting the initial data to

$$T(\xi, 0) = \begin{cases} T_{liq} + \xi(T_{liq})_\xi & \text{and } \lambda_{liq} = \text{const.}, k_{liq} = \text{const. for } \xi < 0, \\ T_{gas} + \xi(T_{gas})_\xi & \text{and } \lambda_{gas} = \text{const.}, k_{gas} = \text{const. for } \xi \geq 0, \end{cases} \quad (36)$$

we can use the solution of the dGRP from the previous section by setting

$$a_{liq/gas} = k_{liq/gas} \text{ and } b_{liq/gas} = \lambda_{liq/gas}. \quad (37)$$

Therefore, we assume a continuous temperature profile and a continuous energy flux and thereby enforce energy conservation. The numerical flux is finally given by

$$\mathbf{F}_{therm}^* = \frac{2\lambda^+\lambda^-(T^+ - T^-)}{\sqrt{\pi\Delta t}(\lambda^+\sqrt{k^-} + \lambda^-\sqrt{k^+})} + \frac{\lambda^+\lambda^-(\sqrt{k^+}T_\xi^+ + \sqrt{k^-}T_\xi^-)}{(\lambda^+\sqrt{k^-} + \lambda^-\sqrt{k^+})}, \quad (38)$$

with the shorthand notation $(*)^+ = (*)_gas$ and $(*)^- = (*)_liq$.

3.4. The Numerical Viscous Flux

The second parabolic flux in the NSE refers to friction. Given the nature of the viscous stress tensor, this problem can not be reduced to one dimension and a straightforward application of the dGRP, as was done for the numerical heat flux, is not possible. Therefore, we follow Gassner et al. [10, 11], in their approach for parabolic systems and extend it to the general liquid/vapor case considered here.

We investigate the viscous Riemann problem normal to the interface defined by the initial conditions (29) and the partial differential equation

$$\frac{\partial \mathbf{U}}{\partial t} - \frac{\partial}{\partial \xi_1} \left(\sum_{j=1}^3 \underline{\underline{D}}_{1j} \frac{\partial}{\partial \xi_j} \mathbf{U} \right) = 0, \quad (39)$$

with the diffusion matrices,

$$\underline{\underline{D}}_{11} = \frac{\mu}{\rho} \begin{pmatrix} 0 & 0 & 0 & 0 & 0 & 0 \\ -\frac{4}{3}v_1 & \frac{4}{3} & 0 & 0 & 0 & 0 \\ -v_2 & 0 & 1 & 0 & 0 & 0 \\ -v_3 & 0 & 0 & 1 & 0 & 0 \\ -\frac{4}{3}(v_1)^2 - (v_2)^2 - (v_3)^2 & \frac{4}{3}v_1 & v_2 & v_3 & 0 & 0 \end{pmatrix},$$

$$\underline{\underline{D}}_{12} = \frac{\mu}{\rho} \begin{pmatrix} 0 & 0 & 0 & 0 & 0 \\ \frac{2}{3}v_2 & 0 & -\frac{2}{3} & 0 & 0 \\ -v_1 & 1 & 0 & 0 & 0 \\ 0 & 0 & 0 & 0 & 0 \\ -\frac{1}{3}v_1v_2 & v_2 & -\frac{2}{3}v_1 & 0 & 0 \end{pmatrix},$$

$$\underline{\underline{D}}_{13} = \frac{\mu}{\rho} \begin{pmatrix} 0 & 0 & 0 & 0 & 0 \\ \frac{2}{3}v_3 & 0 & 0 & -\frac{2}{3} & 0 \\ 0 & 0 & 0 & 0 & 0 \\ -v_1 & 1 & 0 & 0 & 0 \\ -\frac{1}{3}v_1v_3 & v_3 & 0 & -\frac{2}{3}v_1 & 0 \end{pmatrix}.$$

Here, ξ_1 denotes the coordinate into normal direction. Note that the use of the diffusion matrices is equivalent to the standard flux form of the NSE [11].

From here, we further decompose the viscous flux into

$$\mathbf{F}_{visc}^* = \mathbf{F}_{visc,1}^* + \mathbf{F}_{visc,2}^* + \mathbf{F}_{visc,3}^*, \quad (40)$$

where $\mathbf{F}_{visc,1}^* = \mathbf{F}_{visc,1}^*(\mathbf{U}_{\xi_1}^{liq}, \mathbf{U}_{\xi_1}^{gas})$ refers to the flux contribution of the normal gradients and $\mathbf{F}_{visc,2}^* = \mathbf{F}_{visc,2}^*(\mathbf{U}_{\xi_2}^{liq}, \mathbf{U}_{\xi_2}^{gas})$, $\mathbf{F}_{visc,3}^* = \mathbf{F}_{visc,3}^*(\mathbf{U}_{\xi_3}^{liq}, \mathbf{U}_{\xi_3}^{gas})$ the contribution of the tangential gradients. Assuming a continuous tangential gradient contribution, as in [11], leads to an approximation of the tangential contributions as the arithmetic mean of the left and right fluxes

$$\mathbf{F}_{visc,2}^* = \frac{1}{2} \left(\underline{\underline{D}}_{12,liq} \frac{\partial}{\partial \xi_2} \mathbf{U}_{liq} + \underline{\underline{D}}_{12,gas} \frac{\partial}{\partial \xi_2} \mathbf{U}_{gas} \right), \quad (41)$$

$$\mathbf{F}_{visc,3}^* = \frac{1}{2} \left(\underline{\underline{D}}_{13,liq} \frac{\partial}{\partial \xi_3} \mathbf{U}_{liq} + \underline{\underline{D}}_{13,gas} \frac{\partial}{\partial \xi_3} \mathbf{U}_{gas} \right). \quad (42)$$

Note that this assumption is in line with the integral jump conditions across a non-evaporating interface under the neglect of Marangoni forces.

For the normal contribution we can use a more sophisticated approach based on the approach of Gassner et al. [11]. We linearize the diffusion matrix of the normal contribution $\underline{\underline{D}}_{11}$ around a mean state \mathbf{U}_m leading to a linear equation system:

$$\frac{\partial \mathbf{U}}{\partial t} - \frac{\partial}{\partial \xi_1} \left(\underline{\underline{D}}_{11}(\mathbf{U}_m) \frac{\partial}{\partial \xi_1} \mathbf{U} \right) = 0. \quad (43)$$

The linearized diffusion matrix can be diagonalized to the matrix of eigenvalues

$$\underline{\underline{\Lambda}} = \begin{pmatrix} 0 & 0 & 0 & 0 & 0 \\ 0 & \frac{4}{3} \frac{\mu}{\rho^m} & 0 & 0 & 0 \\ 0 & 0 & \frac{\mu}{\rho^m} & 0 & 0 \\ 0 & 0 & 0 & \frac{\mu}{\rho^m} & 0 \\ 0 & 0 & 0 & 0 & 0 \end{pmatrix}, \quad (44)$$

with the corresponding matrix of eigenvectors

$$\underline{\underline{\mathbf{T}}} = \begin{pmatrix} 1 & 0 & 0 & 0 & 0 \\ \frac{m_1^m}{\rho^m} & 1 & 0 & 0 & 0 \\ \frac{m_2^m}{\rho^m} & 0 & 1 & 0 & 0 \\ \frac{m_3^m}{\rho^m} & 0 & 0 & 1 & 0 \\ \frac{E^m}{\rho^m} & \frac{m_1^m}{\rho^m} & \frac{m_2^m}{\rho^m} & \frac{m_3^m}{\rho^m} & 1 \end{pmatrix}, \quad (45)$$

where the superscript m refers to the mean values. The characteristic form of Eq. (43) then follows as

$$\frac{\partial \mathbf{W}}{\partial t} - \frac{\partial}{\partial \xi_1} \left(\underline{\underline{\Lambda}} \frac{\partial}{\partial \xi_1} \mathbf{W} \right) = 0 \quad (46)$$

with the vector of characteristic variables and the vector of their derivatives

$$\mathbf{W} = \underline{\underline{\mathbf{T}}}^{-1} \mathbf{U} \quad \text{and} \quad \frac{\partial}{\partial \xi_1} \mathbf{W} = \underline{\underline{\mathbf{T}}}^{-1} \frac{\partial}{\partial \xi_1} \mathbf{U}. \quad (47)$$

By applying this transformation procedure on both sides of the phase boundary, we obtain a decoupled systems of diffusion problems with discontinuous coefficients normal to the interface. The corresponding generalized diffusive Riemann problem has the initial data

$$\mathbf{W}(\xi_1, 0) = \begin{cases} \mathbf{W}_{liq} + \xi_1 (\mathbf{W}_{\xi_1})_{liq} & \text{for } \xi_1 < 0 \\ \mathbf{W}_{gas} + \xi_1 (\mathbf{W}_{\xi_1})_{gas} & \text{for } \xi_1 \geq 0 \end{cases}. \quad (48)$$

Note that the same transformation matrix is used on both sides of the phase boundary, while the eigenvalue matrix differs and thus introduces discontinuous coefficients. Now, we can use Eq. (27) to obtain the components J_i of the numerical viscous flux by choosing

$$a_{liq/gas} = \Lambda_{ii,liq/gas} \quad \text{and} \quad b_{liq/gas} = \Lambda_{ii,liq/gas} \quad \text{for } i = 1 \dots, 5. \quad (49)$$

They are given by

$$J_i = \frac{2\Lambda_{ii}^+\Lambda_{ii}^-(W_i^+ - W_i^-)}{\sqrt{\pi\Delta t}(\Lambda_{ii}^+\sqrt{\Lambda_{ii}^-} + \Lambda_{ii}^-\sqrt{\Lambda_{ii}^+})} + \frac{\Lambda_{ii}^+\Lambda_{ii}^-(\sqrt{\Lambda_{ii}^+}W_{\xi_1}^+ + \sqrt{\Lambda_{ii}^-}W_{\xi_1}^-)}{(\Lambda_{ii}^+\sqrt{\Lambda_{ii}^-} + \Lambda_{ii}^-\sqrt{\Lambda_{ii}^+})}, \quad (50)$$

where we again use the shorter notation of $(*)^+ = (*)_{\text{gas}}$ and $(*)^- = (*)_{\text{liq}}$. The resulting fluxes are transformed back to the conservative variables by multiplying with the transformation matrix

$$\mathbf{F}_{visc,1}^* = \underline{\mathbf{T}}\mathbf{J}. \quad (51)$$

The total, numerical viscous flux is then given by Eq. (40).

So far we have not discussed the choice of \mathbf{U}_m for the linearization. For small jumps in the coefficients it can be chosen simply as the arithmetic mean of the liquid and vapor states as in [11]. For larger jumps, as is considered in this work, an average state incorporating the different dynamic viscosities is more favorable. We follow the structure of the exact solution at $\xi = 0$ of a scalar dGRP with jumping coefficients and choose

$$\mathbf{U}_m = \frac{\sqrt{\mu_{liq}}\mathbf{U}_{liq} + \sqrt{\mu_{gas}}\mathbf{U}_{gas}}{\sqrt{\mu_{liq}} + \sqrt{\mu_{gas}}}. \quad (52)$$

4. Results

In the present section, numerical results are presented which validate the proposed interfacial Riemann solvers and display their capabilities. We begin with a discussion on the thermal Riemann solver, followed by the viscous solver.

4.1. Thermal Riemann Solver

In the present section, the interfacial heat conduction are validated. Therefore, we employ the well-known test case of Sod in a modified form with two heat conducting fluids. The initial conditions are given by

$$\mathbf{U}(\xi, 0) = \begin{cases} (1, 0, 0, 0, 1)^T & \text{for } \xi < 0, \\ (0.125, 0, 0, 0, 0.1)^T & \text{for } \xi \geq 0. \end{cases} \quad (53)$$

At $\xi = 0$, we position an interface, which separates the two fluids from each other. Each fluid obeys a perfect gas EOS with the specific heat capacity ratio of $\gamma = 1.4$ and a specific heat capacity at constant volume of $c_v = 1$. Although obeying the same equation of state, the two fluids differ in their thermal conductivity with $\lambda = 0.1$ for the fluid left of the interface and $\lambda = 0.001$ for the fluid right of the interface.

No analytical solution is available for this problem, therefore we compare the sharp-interface method with a single-phase DGSEM Navier-Stokes solver [15]. This method is able to consider variable thermal conductivities through the BR1 lifting procedure [17] and is therefore a good reference to validate the novel ghost fluid approach. The solution was obtained with $N_{\text{Elms}} = 200$ solution elements and a polynomial degree of $N = 3$, which was sufficient to achieve grid convergence. We compare this reference solution with the discussed sharp-interface method using the thermal interfacial Riemann solver and the HLLC solver. To focus on the performance of the Riemann solvers we further employ a moving mesh approach for this one-dimensional simulation as was done in [29, 30, 31]. In both simulations we neglect viscous effects.

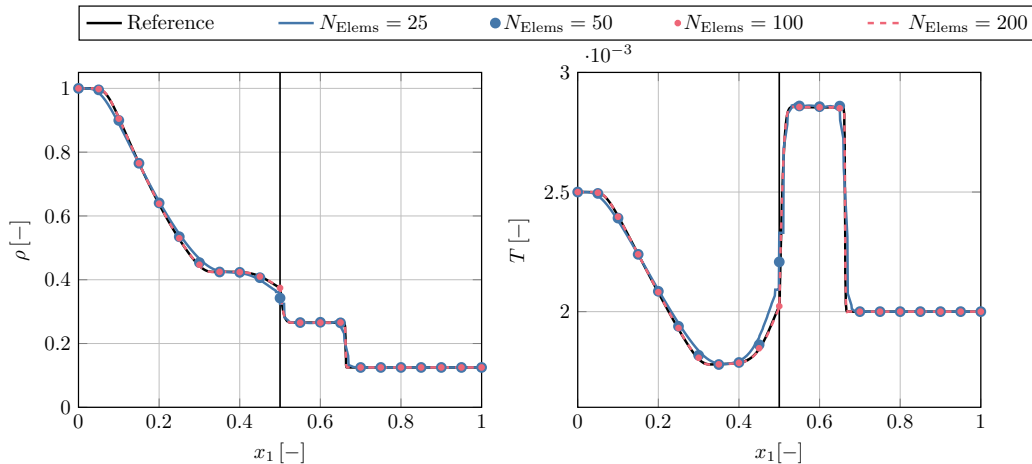


Figure 3: Sod problem with heat conduction after $t = 0.2$. Solutions of the sharp-interface method with the thermal Riemann solver and different meshes are shown compared to a numerical reference solution. The interface is indicated in black.

Four different meshes $N_{\text{Elems}} = 25$, $N_{\text{Elems}} = 50$, $N_{\text{Elems}} = 100$ and $N_{\text{Elems}} = 200$ were used as well as a polynomial degree of $N = 3$. The results are depicted in Fig. 3 at $t = 0.2$. The solution appears to be grid converged with $N_{\text{Elems}} = 100$. The converged solution of the sharp-interface method shows a perfect agreement with the reference data, implying an accurate coupling of the advection and thermal conduction across the interface.

As second test case, we consider a water droplet in air impinging on a water surface, similar to the case in [32]. Here, we focus on the effects of thermal conduction. Droplet, air and water surface are initialized with a different temperature, with the droplet having the hottest temperature and the air the coldest one. A summary of the geometrical setup, is shown in Fig. 4. Gravitation is introduced as an external field and is included as a source term. The water is modeled with a stiffened gas EOS, using $\gamma = 2.51$, a specific

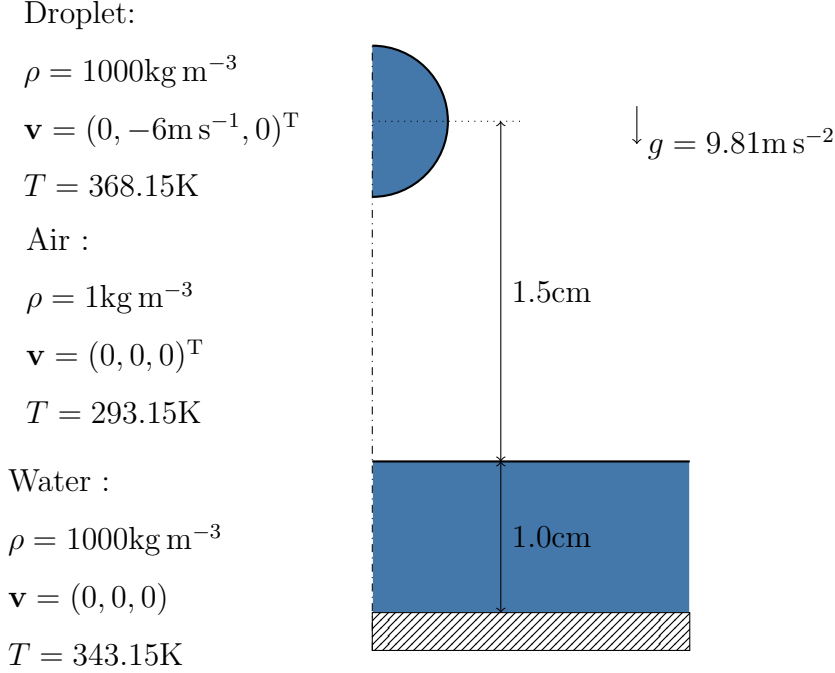


Figure 4: Setup of the impinging droplet test case.

heat capacity ratio at constant pressure of $c_p = 4267 \text{J kg}^{-1} \text{K}^{-1}$, the stiffness parameter $p_\infty = 10^9 \text{Pa}$ and a thermal conductivity of $\lambda = 0.6 \text{W m}^{-1} \text{K}^{-1}$. The air is modeled as a perfect gas with $\gamma = 1.4$, $c_p = 1000 \text{J kg}^{-1} \text{K}^{-1}$ and $\lambda = 0.024 \text{W m}^{-1} \text{K}^{-1}$. The surface tension coefficient was set to $\sigma = 58 \cdot 10^{-3} \text{N m}^{-1}$.

The two-dimensional domain $\Omega \in [0, 3\text{cm}]^2$ was discretized with 120 elements in x_1 direction and 60 elements in x_2 direction. A polynomial degree of $N = 5$ was used. The Lax-Friedrichs Riemann solver was used in the bulk phases. At the interface, the HLLC solver in conjunction with the novel thermal Riemann solver was employed. Viscous effects were neglected. As bound-

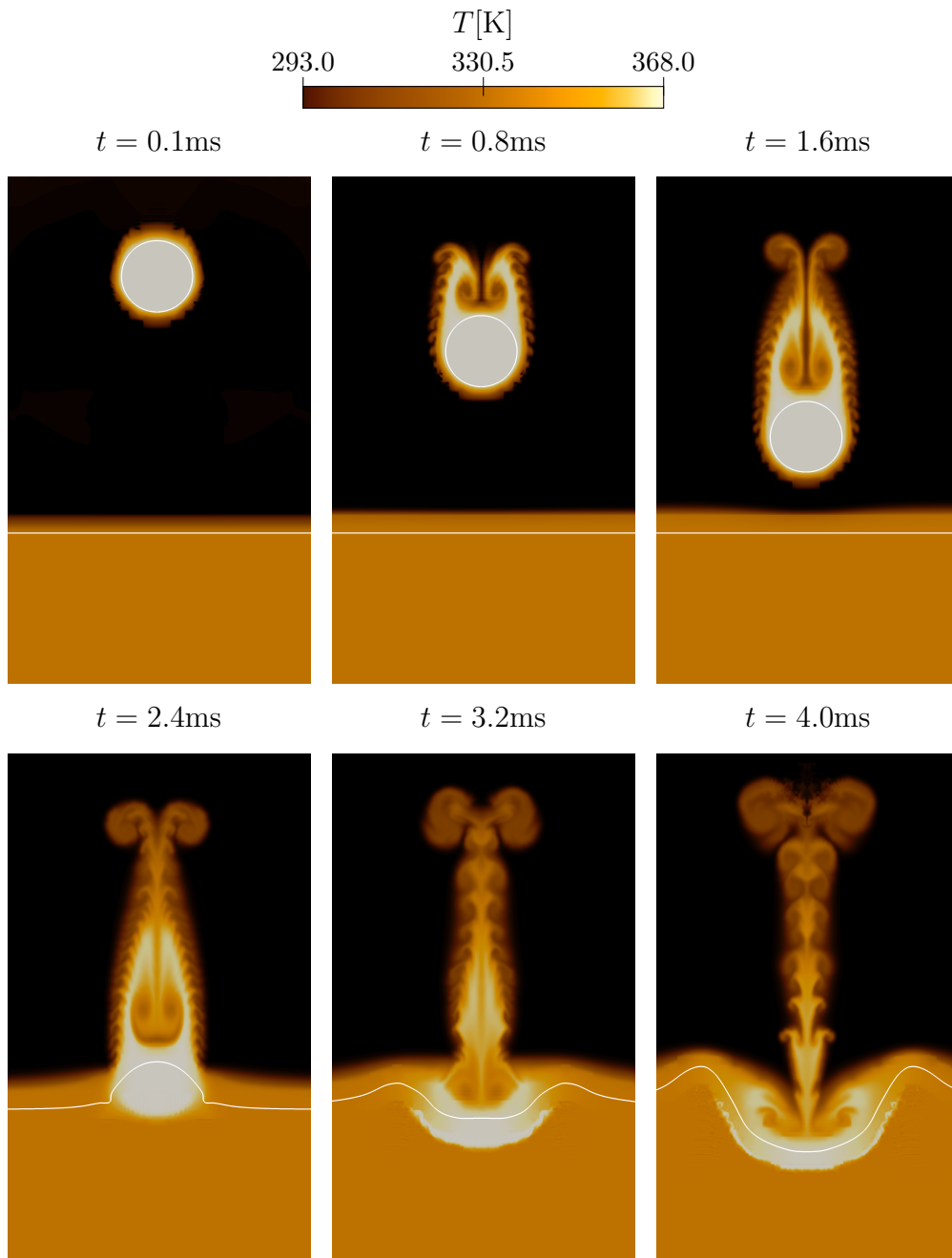


Figure 5: Temperature distribution of the impinging droplet at different time instances. Interfaces are given as a white line.

ary conditions, an Euler wall at the lower boundary was employed while the remaining boundaries used a Dirichlet condition based on the initial data.

The temperature distribution for different time instances is shown in Fig. 5. After $t = 0.1\text{ms}$, the droplet has slightly moved downwards. Heat transfer across the interface induces a heating of the surrounding air. Similar observation can be made at the liquid surface. After $t = 0.8\text{ms}$, a thermal boundary layer at the surface has developed. The droplet moved further downwards and has left a trailing wake of hot air. Therein, buoyancy driven instabilities formed in the areas where hot and cold air meet. After $t = 1.6\text{ms}$, the droplet is very close to the liquid surface. The thermal boundary layer of the liquid surface has been slightly quenched by the incoming pressure waves from the arriving droplet. At $t = 2.4\text{ms}$, the droplet partially merged into the surface, raising the thermal boundary layer. After $t = 3.2\text{ms}$ the droplet is fully engulfed in the liquid surface. Below, the hot liquid starts to spread. The wake above the surface has further cooled and an intricate buoyancy driven flow pattern has emerged. Finally, at $t = 4\text{ms}$, a narrowly defined area of hot air remains in the wake region, in which vortices dominate the flow field. At the droplet's initial position, the onset of a Rayleigh-Taylor instability is visible. Waves on the liquid surface have further traveled away from the center line and the hot liquid from the droplet has now spread almost below the entire visible surface.

The depicted temperature distribution is mainly driven by the interfacial exchange of heat across the interface. The temperature in the air would have been nearly uniform in a simulation without heat conduction. Due to the heating of the air by the droplet, a buoyancy driven flow was induced.

The observations made above are in line with the physical expectations and therefore demonstrate the capability of the proposed method.

4.2. Viscous Riemann Solver

In this section, the viscous Riemann solver is considered. First, we solve a quasi-one-dimensional problem: a multi-material adaption of the first problem of Stokes. A discussion of the original problem can be found in [33, 34]. We choose the initial conditions as follows:

$$(\rho, v_1, v_2, v_3, p) = \begin{cases} (1, 0, -0.1, 0, 1) & \text{for } x_1 < 0, \\ (1, 0, 0.1, 0, 1) & \text{for } x_1 > 0. \end{cases} \quad (54)$$

A different fluid is present at each side of the discontinuity positioned at $x_1 = 0$. As done before, these fluids are described by the same EOS, a perfect gas EOS with $\gamma = 1.4$ and $c_v = 1$. However, they differ in their dynamic viscosity coefficient, given by

$$\mu = \begin{cases} 0.01 & \text{for } x_1 < 0, \\ 0.001 & \text{for } x_1 > 0. \end{cases} \quad (55)$$

Similarly to the original first problem of Stokes, the Navier-Stokes-equations can be reduced to a one-dimensional equation due to the prescribed initial data, reading

$$\frac{\partial v_2}{\partial t} = \mu \frac{\partial^2 v_2}{\partial x_1^2}. \quad (56)$$

Eq. (56) is of the form of Eq. (14). Therefore, the solution of this problem is given by the solution of the dGRP as described in section 3.2.

The modified first problem of Stokes is considered with the present sharp-interface method. The employed two-dimensional computational domain was

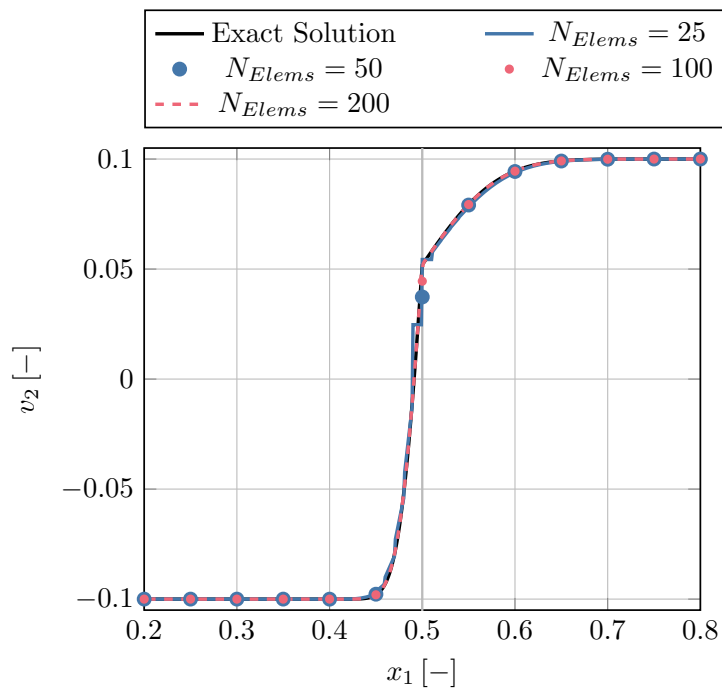


Figure 6: Solution of the modified first problem of Stokes. Comparison of the sharp interface method with the exact solution.

$[0, 1] \times [0, 1]$, where non-reflecting outflow boundaries were employed at the x_1 borders, while periodic boundary conditions were used at the x_2 boundaries. We chose a polynomial degree of $N = 3$, the HLLC solver was applied to calculate the hyperbolic interface flux and the viscous Riemann solver for the parabolic flux. Heat conduction effects were neglected in this case.

The solution of the sharp-interface method as well as the exact solution is shown in Fig. 6 for four different meshes: $N_{Elems} = 25$, $N_{Elems} = 50$, $N_{Elems} = 100$ and $N_{Elems} = 200$ elements. The sharp-interface method shows grid convergence for $N_{Elems} = 100$. Additionally, the numerical results are in perfect agreement with the exact solution.

As a more complex test case, a three-dimensional droplet oscillation is investigated as a second test case. Taken from the work of Lalanne et al. [35], the initial contour of the droplet is given by

$$\psi(\mathbf{x}) = \sqrt{(x_1^2 + x_2^2 + x_3^2)} - R_D \left[1 + 0.15 \left(3 \cos^2 \left(\frac{x_1}{\sqrt{x_1^2 + x_2^2 + x_3^2}} \right) - 1 \right) \right],$$

with the equilibrium droplet radius R_D . The oscillation period of this elongated droplet in air has been studied by Prosperetti [36] and Lamb [37] and is given by

$$T_{osc} = \frac{2\pi \sqrt{R_D^3 (2n\rho_{air} + (n+1)\rho_{liq})}}{\sqrt{\sigma(n-1)n(n+1)(n+2)}}, \quad (57)$$

where n refers to the oscillation mode, with $n = 2$ being the dominating mode. The oscillation of the droplet is damped over time by the effects of viscosity. The decay of the amplitude thereby reads as

$$\frac{r_D(t)}{r_{D,i}(t)} = \exp \left(-t \frac{\mu_{liq} (n-1)(2n+1)}{\rho_{liq} R_D^2} \right), \quad (58)$$

where $r_D(t)$ denotes the time dependent droplet radius and $r_{D,i}(t)$ the theoretical droplet radius in the inviscid case.

In the following, the sharp-interface method is used to simulate such a viscous, oscillating droplet in non-dimensional units. The droplet was positioned inside the center of the computational domain $\Omega \in [-2.5, 2.5]^3$ with a density of $\rho_{liq} = 1000$, a pressure of $P_{liq} = 500$ and a dynamic viscosity of $\mu_{liq} = 10$. The surrounding air was initialized with a density of $\rho_{air} = 1$, a pressure of $P_{air} = 1$ and a dynamic viscosity of $\mu_{air} = 0.01$. The liquid was modeled by a stiffened gas EOS with $\gamma = 4$ and the stiffness parameter $P_\infty = 10^3$. The air was described with a perfect gas EOS using $\gamma = 1.4$. A surface tension coefficient for the liquid-air interface of $\sigma = 250$ was used.

The sharp-interface method used a polynomial degree of $N = 3$ as well as the HLLC solver for the hyperbolic interfacial Riemann problem and the proposed viscous Riemann solver for the parabolic part. Heat conduction was neglected and periodic boundary conditions were used.

The temporal variation of the droplet radius on the x_1 -axis is depicted in Fig. 7 for three different mesh sizes $N_{Elems} = 10^3$, $N_{Elems} = 20^3$ and $N_{Elems} = 30^3$ and the theoretically predicted envelope of the oscillation frequency from Eq. (58). The results clearly show a convergence of the scheme towards the theoretical prediction, both in the oscillation frequency as well as the damping rate. Over time, the oscillation frequency reduces and the damping increases. This is an effect of an increased numerical dissipation induced by the bulk phase Riemann solvers for the present low-speed problem, as was discussed by Zeifang and Beck [32]. Therefore, the precise prediction of the damping rate in the first oscillation period is a strong indication for the validity of the proposed method.

Finally, we simulated a 2D shock-droplet interaction in the shear-induced entrainment (SIE) regime with Weber number $We = 7339$ inspired by Winter et al. [38]. Initially, a droplet with the diameter of $D_0 = 1\text{m}$ is positioned at $(x, y) = (0, 0)$ inside the computational domain $\Omega = [-2D_0, 10D_0] \times [0, 3D_0]$, with D_0 being the droplet radius. The surrounding air is at rest. A right-moving shock wave, with Mach number $Ma = 1.47$, is placed at $x = -D_0$. Hence, at the left boundary a Dirichlet boundary condition is imposed based on the post shock state. The lower boundary is set as a symmetry plane and the remaining boundaries are treated with non-reflective outflow conditions. A summary of the initial conditions and material parameters is given in Table

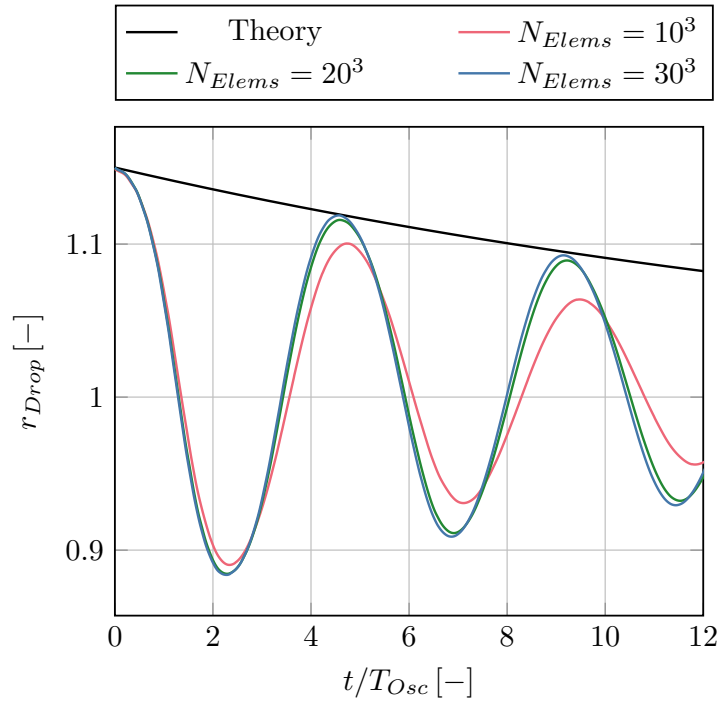


Figure 7: Droplet radius oscillation on the x_1 -axis over several oscillation periods supplemented by the envelope of the analytically predicted damped radius.

1. The initial pressure difference between the droplet and air was defined by the Young-Laplace Law

$$\Delta p = \frac{2\sigma}{D_0}. \quad (59)$$

The dynamic viscosities of water and air were calculated by using the Ohnesorge number

$$\text{Oh} = \frac{\mu_{liq}}{\sqrt{\rho_{liq} D_0 \sigma}}, \quad (60)$$

the Weber number

$$\text{We} = \frac{\rho_{gas} u_{gas}^2 D_0}{\sigma}, \quad (61)$$

and the Reynolds number

$$\text{Re} = \frac{\rho_{gas} u_{gas} D_0}{\mu_{gas}}. \quad (62)$$

Following in Winter et al. [38], the Ohnesorge number is taken as $\text{Oh} = 6.9 \times 10^{-3}$ and the Reynolds number as $\text{Re} = 229485$.

Fluid	$p_0[\text{Pa}]$	$\rho_0[\text{kg m}^{-3}]$	$\gamma[-]$	$p_\infty[\text{GPa}]$	$\mu[10^{-2}\text{Pa s}]$	$\sigma[10^{-2}\text{kg s}^{-2}]$
Air	101325	1.204	1.4	0	0.011	
Water	101325.146	1000	6.12	0.343	5.885	7.28

Table 1: Initial conditions and material parameters for the shock-droplet interaction

The domain was discretized with 512×256 elements. The polynomial degree of the DG solution was $N = 3$. We used the HLLC Riemann solver in the bulk and an explicit 4th order Runge-Kutta time stepping scheme. At the interface, the HLLC solver and the viscous Riemann solver was employed. Heat conduction was neglected in the entire domain. A time series of the

obtained results is given in Figure 8. The solution is plotted at the non-dimensional time

$$t^* = \frac{t}{\frac{D_0}{u_s} \sqrt{\frac{\rho_{liq}}{\rho_s}}} \quad (63)$$

with u_s and ρ_s denoting the post-shock velocity and density of air. Figure 8 shows the numerical Schlieren and non-dimensional streamwise velocity $u^* = u/u_s$ at $t^* = 0.25$, $t^* = 0.5$ and $t^* = 1.0$. Due to the striking of the shock wave and the acceleration of the air, the droplet deforms. Separation of the flow from the droplet surface results in the shedding of vortices. Comparing the present results to the ones given by Winter et al. [38], the droplet deformation and generated vortical structures agree very well with each other.

5. Conclusion

In the present work we discussed a novel approach based on Riemann-solvers for the consideration of heat conduction and friction at sharp-interfaces. We extended the ghost fluid method by defining the interfacial fluxes as the sum of the hyperbolic flux and the two parabolic fluxes, similar to the typical single-fluid case. Each of the fluxes is individually defined by a Riemann solver. We employed the well-known HLLC solver for the hyperbolic flux and formulated novel solvers based on the diffusive generalized Riemann problem. For the thermal Riemann problem, we were able to simplify the problem to a scalar equation and thus derived an exact interfacial thermal flux. Such an approach is not possible for the viscous Riemann problem, for which we derived an approximate solution based on a linearization of the diffusion matrix.

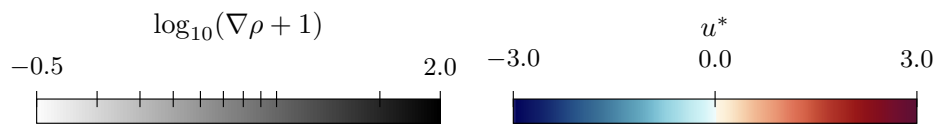
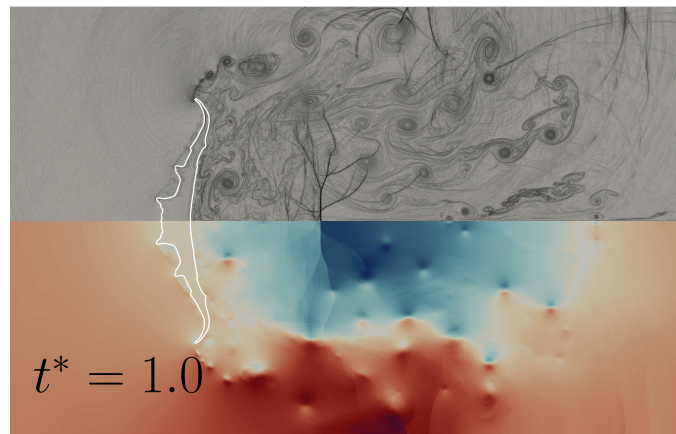
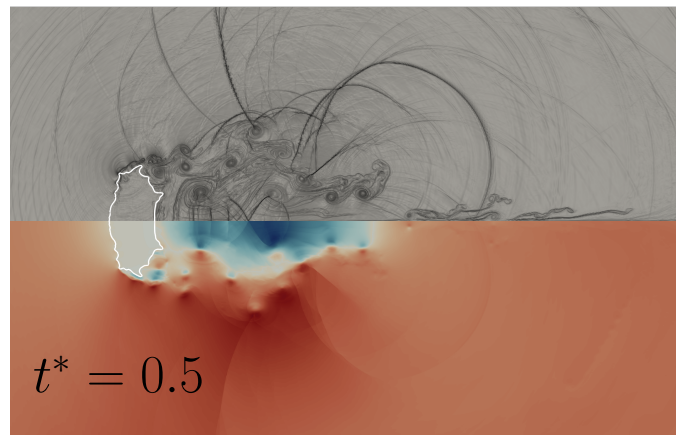
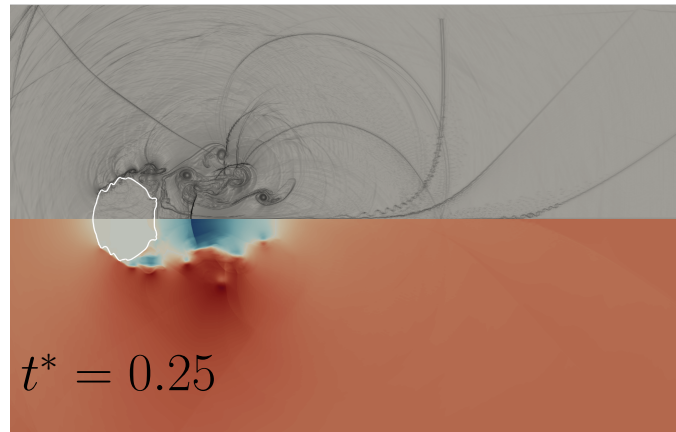


Figure 8: Shock-droplet interaction with numerical Schlieren at the top, non-dimensional streamwise velocity u^* at the bottom. The interface is displayed as a white line.

The novel Riemann solvers were employed in a compressible sharp-interface level-set ghost fluid method. The fluid flow in the bulk phases was solved with the DGSEM with finite volume shock capturing. We studied one-dimensional problems dominated by heat conduction and friction and observed an excellent agreement of our approach with the employed reference data. Additionally, we investigated the viscous damping of an oscillating droplet, for which our scheme was able to recover the theoretical predictions. The robustness and applicability of the numerical scheme was demonstrated in two separate cases: a heated falling droplet impinging on a water surface and a shock-droplet interaction in the shear-induced entrainment regime.

Future investigations of the proposed method should focus on a comparing it with other well-known approaches. Further, other parabolic effects, e.g. species diffusion, could be easily included by following the outline of the present work. Finally, we want to use the inclusion of viscous and thermal effects in the study of droplet grouping effects.

6. Acknowledgements

The authors also kindly acknowledge the financial support provided by the German Research Foundation (DFG) through the Project SFB-TRR 75, Project number 84292822 - “Droplet Dynamics under Extreme Ambient Conditions”, the GRK 2160/1 ”Droplet Interaction Technologies” under the project number 270852890 as well as Germany’s Excellence Strategy - EXC 2075 – 390740016. The simulations were performed on the national supercomputer HPE APOLLO (HAWK) at the High Performance Computing Center Stuttgart (HLRS) under the grant number hpcmphas/44084.

References

- [1] R. P. Fedkiw, T. Aslam, B. Merriman, S. Osher, A non-oscillatory Eulerian approach to interfaces in multimaterial flows (the ghost fluid method), *Journal of Computational Physics* 152 (1999) 457–492. doi:10.1006/jcph.1999.6236.
- [2] C. Hirt, B. Nichols, Volume of fluid (VOF) method for the dynamics of free boundaries, *Journal of Computational Physics* 39 (1981) 201–225. doi:10.1016/0021-9991(81)90145-5.
- [3] G. Tryggvason, B. Brunner, A. Esmaeeli, D. Juric, N. Al-Rawahi, W. Tauber, J. Han, S. Nas, Y.-J. Jan, A front-tracking method for the computations of multiphase flow, *Journal of Computational Physics* 169 (2001) 708–759. doi:10.1006/jcph.2001.6726.
- [4] M. Sussman, P. Smereka, S. Osher, A level set approach for computing solutions to incompressible two-phase flow, *Journal of Computational Physics* 114 (1994) 146–159. doi:10.1006/jcph.1994.1155.
- [5] R. P. Fedkiw, X.-D. Liu, The ghost fluid method for viscous flows, in: *Innovative Methods for Numerical Solution of Partial Differential Equations*, WORLD SCIENTIFIC, 2001, pp. 111–143. doi:10.1142/9789812810816_0005.
- [6] J. U. Brackbill, D. B. Kothe, C. Zemach, A continuum method for modeling surface tension, *Journal of Computational Physics* 100 (1992) 335–354. doi:10.1016/0021-9991(92)90240-Y.

- [7] T. Liu, B. Khoo, K. Yeo, Ghost fluid method for strong shock impacting on material interface, *Journal of Computational Physics* 190 (2003) 651–681. doi:10.1016/s0021-9991(03)00301-2.
- [8] C. Merkle, C. Rohde, The sharp-interface approach for fluids with phase change: Riemann problems and ghost fluid techniques, *ESAIM: Mathematical Modelling and Numerical Analysis* 41 (2007) 1089–1123. doi:10.1051/m2an:2007048.
- [9] S. Fechter, C.-D. Munz, C. Rohde, C. Zeiler, Approximate Riemann solver for compressible liquid vapor flow with phase transition and surface tension, *Computers & Fluids* 169 (2018) 169–185. doi:10.1016/j.compfluid.2017.03.026.
- [10] G. Gassner, F. Lörcher, C.-D. Munz, A contribution to the construction of diffusion fluxes for finite volume and discontinuous Galerkin schemes, *Journal of Computational Physics* 224 (2007) 1049–1063. doi:10.1016/j.jcp.2006.11.004.
- [11] G. Gassner, F. Lörcher, C.-D. Munz, A discontinuous Galerkin scheme based on a space-time expansion II. Viscous flow equations in multi dimensions, *Journal of Scientific Computing* 34 (2007) 260–286. doi:10.1007/s10915-007-9169-1.
- [12] F. Lörcher, G. Gassner, C.-D. Munz, An explicit discontinuous Galerkin scheme with local time-stepping for general unsteady diffusion equations, *Journal of Computational Physics* 227 (2008) 5649–5670. doi:10.1016/j.jcp.2008.02.015.

- [13] S. Jöns, C. Müller, J. Zeifang, C.-D. Munz, Recent advances and complex applications of the compressible ghost fluid method, SEMASIMAI Springer Series, Proceedings of Numhyp 2019. accepted. Springer, (2020).
- [14] F. Hindenlang, G. J. Gassner, C. Altmann, A. Beck, M. Staudenmaier, C.-D. Munz, Explicit discontinuous Galerkin methods for unsteady problems, *Computers & Fluids* 61 (2012) 86–93. doi:10.1016/j.compfluid.2012.03.006.
- [15] N. Kraus, A. Beck, T. Bolemann, H. Frank, D. Flad, G. Gassner, F. Hindenlang, M. Hoffmann, T. Kuhn, M. Sonntag, C.-D. Munz, FLEXI: A high order discontinuous Galerkin framework for hyperbolic–parabolic conservation laws, *Computers & Mathematics with Applications* (2020). doi:10.1016/j.camwa.2020.05.004.
- [16] M. Sonntag, C.-D. Munz, Efficient parallelization of a shock capturing for discontinuous Galerkin methods using finite volume sub-cells, *Journal of Scientific Computing* 70 (2016) 1262–1289. doi:10.1007/s10915-016-0287-5.
- [17] F. Bassi, S. Rebay, A high-order accurate discontinuous finite element method for the numerical solution of the compressible navier–stokes equations, *Journal of Computational Physics* 131 (1997) 267–279. doi:10.1006/jcph.1996.5572.

- [18] C. A. Kennedy, M. H. Carpenter, Additive runge–kutta schemes for convection–diffusion–reaction equations, *Applied Numerical Mathematics* 44 (2003) 139–181. doi:10.1016/s0168-9274(02)00138-1.
- [19] M. Dumbser, R. Loubère, A simple robust and accurate a posteriori sub-cell finite volume limiter for the discontinuous galerkin method on unstructured meshes, *Journal of Computational Physics* 319 (2016) 163–199. doi:10.1016/j.jcp.2016.05.002.
- [20] S. Fechter, Compressible Multi-Phase Simulation at Extreme Conditions Using a Discontinuous Galerkin Scheme, Ph.D. thesis, 2015. doi:10.18419/opus-3982.
- [21] D. Peng, B. Merriman, S. Osher, H. Zhao, M. Kang, A PDE-based fast local level set method, *Journal of Computational Physics* 155 (1999) 410–438. doi:10.1006/jcph.1999.6345.
- [22] L. Xu, T. Liu, Accuracies and conservation errors of various ghost fluid methods for multi-medium Riemann problem, *Journal of Computational Physics* 230 (2011) 4975–4990. doi:10.1016/j.jcp.2011.03.021.
- [23] L. Xu, C. Feng, T. Liu, Practical Techniques in Ghost Fluid Method for Compressible Multi-Medium Flows, *Commun. Comput. Phys.* 20 (2016) 619–659. doi:10.4208/cicp.190315.290316a.
- [24] S. Fechter, C.-D. Munz, A discontinuous Galerkin-based sharp-interface method to simulate three-dimensional compressible two-phase flow, *International Journal for Numerical Methods in Fluids* 78 (2015) 413–435. doi:10.1002/flid.4022.

- [25] F. Föll, C. Müller, J. Zeifang, C.-D. Munz, A novel regularization strategy for the local discontinuous galerkin method for level-set reinitialization, arXiv preprint arXiv:2007.06883 (2020).
- [26] E. F. Toro, M. Spruce, W. Speares, Restoration of the contact surface in the HLL-Riemann solver, *Shock Waves* 4 (1994) 25–34. doi:10.1007/bf01414629.
- [27] X. Hu, N. Adams, G. Iaccarino, On the HLLC Riemann Solver for Interface Interaction in Compressible Multi-Fluid Flow, *Journal of Computational Physics* 228 (2009) 6572–6589. doi:10.1016/j.jcp.2009.06.002.
- [28] F. Jaegle, C. Rohde, C. Zeiler, A multiscale method for compressible liquid-vapor flow with surface tension, *ESAIM: Proceedings* 38 (2012) 387–408. doi:10.1051/proc/201238022.
- [29] T. Hitz, S. Jöns, M. Heinen, J. Vrabec, C.-D. Munz, Comparison of macro- and microscopic solutions of the Riemann problem II. Two-phase shock tube, *Journal of Computational Physics* 429 (2021) 110027. doi:10.1016/j.jcp.2020.110027.
- [30] S. Jöns, C.-D. Munz, Riemann solvers for phase transition in a compressible sharp-interface method, *Applied Mathematics and Computation* 440 (2023) 127624.
- [31] C. Müller, P. Mossier, C.-D. Munz, A sharp interface framework based on the inviscid godunov-peshkov-romenski equations: Simulation of evaporating fluids, *Journal of Computational Physics* 473 (2023) 111737.

- [32] J. Zeifang, A. Beck, A low mach number imex flux splitting for the level set ghost fluid method, *Communications on Applied Mathematics and Computation* (2021) 1–29.
- [33] H. Schlichting, K. Gersten, *Boundary-Layer Theory*, volume 7, Springer Berlin Heidelberg, Berlin, Heidelberg, 2017. doi:10.1007/978-3-662-52919-5.
- [34] M. Dumbser, I. Peshkov, E. Romenski, A unified hyperbolic formulation for viscous fluids and elastoplastic solids, in: *Theory, Numerics and Applications of Hyperbolic Problems II*, Springer International Publishing, 2018, pp. 451–463. doi:10.1007/978-3-319-91548-7_34.
- [35] B. Lalanne, L. Rueda Villegas, S. Tanguy, F. Risso, R. Villegas, On the computation of viscous terms for incompressible two-phase flows with Level Set/Ghost Fluid Method On the computation of viscous terms for incompressible two-phase flows with Level Set/Ghost Fluid Method Open Archive TOULOUSE Archive Ouverte (OATAO), *Journal of Computational Physics* 301 (2015) 289–307. doi:10.1016/j.jcp.2015.08.036i.
- [36] A. Prosperetti, Normal-mode analysis for the oscillations of a viscous liquid drop in an immiscible liquid, *J. Mecanique* 19 (1980) 149–182.
- [37] H. Lamb, *Hydrodynamics*, University Press, 1924.
- [38] J. Winter, J. Kaiser, S. Adami, N. Adams, Numerical investigation of 3d drop-breakup mechanisms using a sharp interface level-set method, in: *11th International Symposium on Turbulence and Shear Flow Phenomena, TSFP 2019*, 2019.